21st Australasian Fluid Mechanics Conference
Adelaide, Australia
10-13 December 2018

Two-dimensional Axisymmetric Simulation of Under-expanded Supersonic Impinging Jet

M. Li[1], J. Soria[2] and A. Ooi[1]

[1]Department of Mechanical Engineering
University of Melbourne, Victoria 3010, Australia

[2]Laboratory for Turbulence Research in Aerospace & Combustion
Department of Mechanical and Aerospace Engineering
Monash University, Victoria 3800, Australia

Abstract

This paper investigates the unsteady flow features of two-dimensional (2D) axisymmetric under-expanded supersonic impinging jet with a nozzle pressure ratio (*NPR*) of 3.5 and a distance ratio (*z/D*) of 2.5. A comparison between 2D axisymmetric, three-dimensional (3D) Large Eddy Simulation (LES) and experimental data is given. Good agreement can be seen in mean profiles and shock location data. Utilizing spectral and Proper Orthogonal Decomposition (POD) tools, two acoustic contributions of the 2D axisymmetric simulation are observed at the dominant tone frequency. The first one is responsible for acoustic waves propagating to the far field and the other one observed from the sides of the jet plume contributes to the feedback mechanism. Furthermore, the oscillation of the stand-off shock may be one of the triggers of the feedback mechanism of 2D axisymmetric simulation, which is consistent with Henderson and Powell's hypothesis[4].

Introduction

Under-expanded supersonic impinging jets which generate highly unsteady flows have been investigated for over 70 years. Marsh [7] found the discrete tones for subsonic impinging jets, followed by Ho and Nosseir [5] who investigated moderate to highly compressible flows. The well-known hydrodynamic-acoustic feedback mechanism model of impinging tone was first proposed by Powell [9], while this model only accounts for the sound source on the plate in the wall jet region. Explanations for the feedback mechanism are still the subject of debate due to the complexity of the flow structure. Henderson and Powell [4] were still in doubt that the oscillation of the stand-off shock is a part of the feedback loop. Henderson [3] suggested the appearance of second local maximum pressure on the plate as the sound source. However, Ho and Nosseir [5] hypothesized that the discrete tone may be produced by the interaction between vortical structures and the impinging plate. In recent studies, Weightman *et al.* [13] conducted an experiment with ultra-high-speed Schileren and found that a periodic transient weak shock on the plate is responsible for the generation of discrete tones. They stated that the mechanism produced by this shocklet is independent of geometry. Wilke and Sesterhenn [14] conducted a DNS at Reynolds number of 3300 and found that the interaction between vortical structures and the stand-off shock is responsible for the feedback mechanism. In regard to 2D axisymmetric simulation, Zang *et al.*[15] who performed both 2D axisymmetric and full 3D RANS simulations of the under-expanded supersonic jet, found good agreement with experiment in mean profiles and shock locations. Kim and Park [6] utilized unsteady axisymmetric simulations with different distance ratios and *NPR*s, and found that the staging behavior is in agreement with experimental results. The aim of this paper is first to investigate if important steady and unsteady features of the under-expanded impinging jet can be reproduced by the unsteady 2D axisymmetric simulation. In addition, a possible cause of the feedback mechanism of the 2D axisymmetric simulation is suggested.

Methodology

Jet and numerical parameters

The configuration of current simulations is consistent with the experimental studies by Risborg [10]. The nozzle is characterized by nozzle exit diameter (D), lip thickness *0.3D* and contraction ratio 64. An impinging plate is placed normal to the direction of nozzle exit at a distance of *2.5D*. The nozzle pressure ratio ($NPR = p_0/p_{atm}$) is 3.5, where p_0 is the stagnation pressure and p_{atm} is the ambient pressure. A non-reflective pressure boundary condition is applied in the far field to avoid pressure reflections from the outlet. The stagnation temperature is the same as the ambient temperature of $293K$. No-slip and adiabatic conditions are applied to the velocity and the temperature at both the nozzle wall and the impinging plate, respectively. The nozzle exit Mach number ($M_e = U_e/a_e$) is 1, where U_e is the nozzle exit velocity and a_e is the sonic speed at nozzle exit. Mesh resolution of the current 3D LES is equivalent with that of Dauptain *et al.*[2] and the mesh for the 2D axisymmetric simulation has been determined to be independent of the grid. The current numerical method utilizes a density-based, transient, central-upwind compressible solver. The temporal integration and the spatial discretization are implemented with the second-order backward Euler and the second-order central difference schemes, respectively.

Governing equations

2D axisymmetric governing equations are described in cylindrical form (x,z) as,

$$\frac{\partial A}{\partial t}+\frac{\partial B}{\partial z}+\frac{\partial C}{\partial x}+\frac{1}{x}D=0 \tag{1}$$

where

$$A=\begin{bmatrix}\rho\\ \rho u_z\\ \rho u_x\\ \rho e\end{bmatrix}$$

$$B=\begin{bmatrix}\rho u_z\\ \rho u_z u_z+p-\tau_{zz}\\ \rho u_z u_x-\tau_{xz}\\ (\rho e+p)u_z-u_z\tau_{zz}-u_x\tau_{zx}+q_z\end{bmatrix}$$

$$C=\begin{bmatrix}\rho u_x\\ \rho u_x u_z-\tau_{xz}\\ \rho u_x u_x+p-\tau_{xx}\\ (\rho e+p)u_x-u_z\tau_{xz}-u_x\tau_{zx}+q_x\end{bmatrix}$$

$$D=\begin{bmatrix}\rho u_x\\ \rho u_x u_z-\tau_{zx}\\ \rho u_x u_x-\tau_{xx}\\ (\rho e+p)u_x-u_z\tau_{zx}-u_x\tau_{xx}+q_x\end{bmatrix},$$

where u_z is the stream-wise velocity; u_x is the radial velocity; ρ is the density of the ideal gas; viscous stresses are: $\tau_{zz} = \frac{2}{3}\mu(2\frac{\partial u_z}{\partial z} - \frac{\partial u_x}{\partial x})$, $\tau_{xx} = \frac{2}{3}\mu(2\frac{\partial u_x}{\partial x} - \frac{\partial u_z}{\partial z})$ and $\tau_{xz} = \tau_{zx} = \mu(\frac{\partial u_z}{\partial x} + \frac{\partial u_z}{\partial x})$; μ is the viscous viscosity; e is the total energy; heat flux: $q_z = -\frac{\mu}{Pr(\Gamma-1)}\frac{\partial T}{\partial z}$ and $q_x = -\frac{\mu}{Pr(\Gamma-1)}\frac{\partial T}{\partial x}$; T is the flow temperature; Pr is the Prandtl number, which is chosen to be 0.7 for current simulations. Considering perfect gas flow condition, equations above are closed by $p = \rho RT$.

Current Large Eddy Simulation (LES) adopts the classic compressible Smagorinsky model because it was successfully validated by Chan *et al.* [1] and Dauptain *et al.* [2] in regard to supersonic impinging jets. This model is based on eddy viscosity and eddy diffusivity hypotheses. The eddy viscosity can be written as,

$$\mu^{sgs} = \overline{\rho} C_k \Delta (k^{sgs})^{1/2}, \tag{2}$$

where C_k is the model constant with value 0.094, Δ is the sub-grid length scale and k^{sgs} is the sub-grid scale kinetic energy.

Then the density-weighted sub-grid scale stress and heat flux can be written as,

$$\tau^{sgs} = \frac{2}{3}\overline{\rho} k^{sgs}\delta_{ij} - 2\mu^{sgs}(\widetilde{S_{ij}} - \frac{1}{3}\delta_{ij}\widetilde{S_{kk}}) \tag{3}$$

$$q_j^{sgs} = -\kappa^{sgs}\frac{\partial \widetilde{T}}{\partial x_i}, \tag{4}$$

where $\widetilde{S_{ij}}$ is the filtered strain rate; δ_{ij} is the Kronecker delta; $\widetilde{T}$ is the filtered temperature; κ^{sgs} is the eddy diffusivity which is defined as $\kappa^{sgs} = \mu^{sgs}/Pr_t$.

The model assumes the local equilibrium between sub-grid scale energy production and dissipation which is shown as,

$$\widetilde{S_{ij}} : \tau^{sgs} + C_e\overline{\rho}(k^{sgs})^{1.5} = 0, \tag{5}$$

where C_e is the constant for dissipation; : is the double inner product. Then the final form of eddy viscosity model can be written as,

$$\mu^{sgs} = \overline{\rho}(C_s\Delta)^2\sqrt{2\widetilde{S_{ij}}\widetilde{S_{ij}}}, \tag{6}$$

where Smagorinsky model constant $C_s = (C_k^3/C_e)^{1/4}$.

Proper Orthogonal Decomposition (POD)

Proper Orthogonal Decomposition (POD) [12] is a method for investigating dominant flow features. Since flow dynamics and shock oscillations of under-expanded jets contain a large amount of kinetic energy, it is expected that POD will be able to capture the most energetic spatial distributions of the flow field. In the current study, the POD is performed based on the velocity fluctuation fields.

Results and Discussions

Validation of axisymmetric and 3D LES simulation

Figure 1 shows the comparison of time-averaged density gradient profiles. Figure 1(a) is the experimental shadowgraph from Risborg[10], whilst Figure 1(b) shows current numerical simulations in which the left half is axisymmetric data and the right half is 3D LES data. It can be seen that both simulations can capture the shear layer in the first half of the first shock cell and are almost identical with each other. In addition, a Mach disk and a stand-off shock can be observed from both simulations, which are consistent with the experimental data. The main difference between axisymmetric and 3D data is reflected by the slightly lower intensity of the density gradient of the axisymmetric simulation. Similar trends can also be found in the mean pressure and velocity profiles, which are not shown here due to the page constraint.

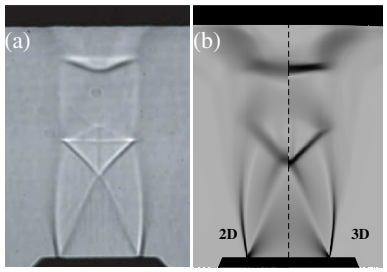

Figure 1: Comparison between experimental and simulation data, where (a) is shadowgraph from Risborg [10], whilst the left half of (b) is the mean density gradient profile of 2D axisymmetric data and the right half is 3D LES data.

Figure 2 shows the non-dimensionalized centerline mean density and Mach number, where 2D axisymmetric and 3D LES data are plotted with the black and gray lines, respectively. The overlaid diamond and circle in Figure 2 show the locations of Mach disk and stand-off shock. Shock locations are defined as the place of the local maximum density gradient. It can be seen that the mean non-dimensionalized density and Mach number are overlapped with distance ratio less than 1 (i.e. $z/D \leq 1$). Although differences between 2D and 3D data appear afterward, trends in axisymmetric and 3D data are similar in both figures. In addition, comparison of Mach disk locations among the current two simulations and another 3D LES with the same jet parameters from Chan *et al.* [1] are shown in Table 1. It can be seen that shock locations from these three simulations are consistent with [10], while the current 3D LES simulation with density-based solver behaves slightly better than that with PISO algorithm [1].

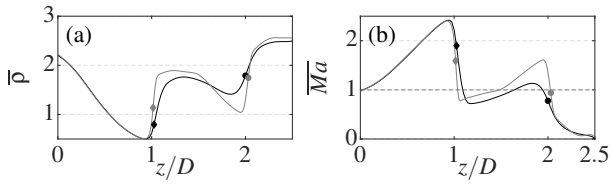

Figure 2: Comparison of mean normalized centerline density(a) and Mach number (b) between 2D axisymmetric simulation and 3D LES data, in which ——: 2D axisymmetric data; ——: 3D LES data. ◊ and ○ indicate the locations of Mach disk and stand-off shock, respectively. The horizontal black dash line of (b) indicates the choked Mach number.

Experiment [10]	3D LES [1]	3D LES (C)	2D axi (C)
—	1.45	1.40	2.40

Table 1: Percentage errors of Mach disk location compared with experimental data from Risborg [10]. 'C' indicates current simulations.

Spectral and POD analysis of 2D axisymmetric simulation

Figure 3 shows the near-field acoustic spectrum represented by the sound pressure level (SPL) as a function of frequency. A probe is placed at *x/D = 1, z/D = 0.* The acoustic spectrum is calculated by a sliding window with *50%* overlap and Hanning

window function. It is observed that two discrete tones with frequency $f_1 = 36132Hz$ and $f_2 = 26367Hz$ exceed the broadband noise at least *5dB*, where f_1 is the dominant tone frequency and f_2 is the secondary tone frequency. Figure 4 shows the amplitudes of pressure fluctuation fields for the two frequencies to reveal the contributions of the acoustic feedback. In Figure 4(a), both shock locations can be observed. One acoustic contribution can be approximately found along the sides of the jet core region. In addition, a second local maximum pressure can be observed at around *x/D = 1.3*, which is responsible for the acoustic generation [3]. The location is also consistent with the findings by Chan *et al.* [1]. Turning to Figure 4(b), two acoustic contributions can be identified. The first one is responsible for closing the feedback along the sides of the jet plume and the other one located on the plate at around *x/D = 2* is responsible for acoustic waves mainly propagating to the far field.

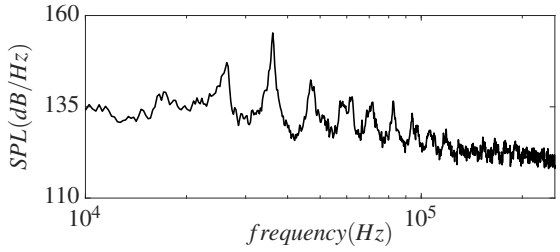

Figure 3: Acoustic spectra at probe location (*x/D = 1, z/D = 0*).

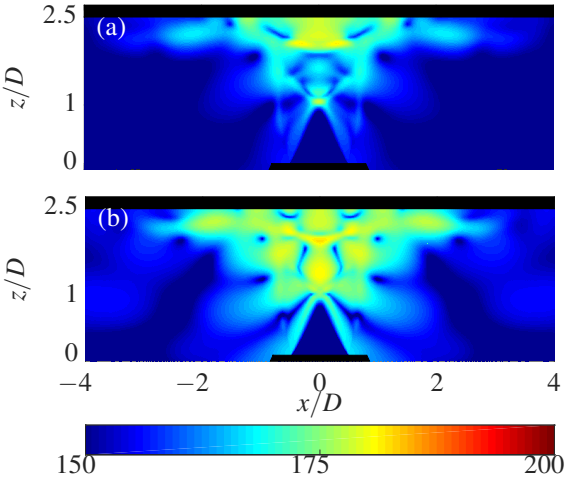

Figure 4: Magnitudes of pressure fluctuation fields for the secondary tone frequency (a) and the dominant tone frequency (b) ranging from *100* to *145 dB*.

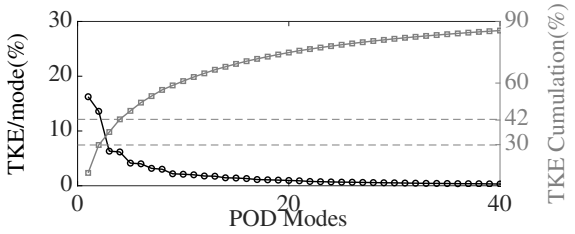

Figure 5: Turbulent kinetic energy (TKE) per mode and cumulative energy of the first 40 modes in percentage where ——: TKE/mode and ——: TKE cumulation.

Figure 5 shows the distribution of turbulent kinetic energy (TKE) of each mode and the accumulative TKE of the first 40 POD modes. It can be seen that the first 40 modes contain around 86% TKE in total, where the first four modes contain around 16.3%, 13.6%, 6.5% and 6.4% energy respectively. Each of the rest modes contains less than 4% of total TKE and thus will be omitted in the following analysis. To investigate the relationship between these four modes, joint PDFs of the normalized temporal coefficients with overlaid Lissajous lines are shown in Figure 6. It is observed that the Lissajous line of the first two modes is similar to a circle, which implies the first two modes are at same frequency but with a 90 degree phase shift, while the modal pair between the mode 1 and the mode 3 or the mode 4 are the higher harmonics of the first pair [8]. Figure 7 shows the first four POD modes in the radial (x) and stream-wise (z) velocity fields respectively. It is anticipated that the radial profiles of the first two modes in Figure 7(a) have a similar appearance with a certain phase shift as those of mode 3 and mode 4 in Figure 7(b). This is consistent with the temporal behavior of Figure 6. It can also be found that the first four modes in the stream-wise velocity field enable the detection of the first shock location, while only the first two modes can capture large oscillations of the stand-off shock. Thus, it is interesting to investigate the relationship between the most energetic POD mode structures and the cause of the discrete tone generation. Figure 8 shows the fast Fourier transform (FFT) of the first four most energetic POD temporal coefficients. It can be seen that the first two coefficients show that this dominant frequency equals the dominant tonal frequency which was obtained previously. This implies that the first two POD modes are driven by this dominant frequency. To reiterate, only the first two modes can capture the large oscillation of stand-off shock. Therefore, one of the possible triggers of the acoustic generation is the stand-off shock oscillation, which is consistent with Henderson and Powell's hypothesis [4]. It is necessary to note that the magnitudes of the temporal coefficients of the last two modes contain around one-fifth of the magnitude of the mode 1 coefficient, thus it is not definite to eliminate the relationship between the acoustic contribution and the mode 3 or mode 4. This uncertainty may be improved by implementing Dynamic Mode Decomposition (DMD) [11] to study the dominant flow structures by certain frequencies.

Conclusion

For the current study, results from 2D axisymmetric simulation are shown to be comparable to the 3D LES and experimental data when comparing mean profiles, shock locations, and centerline normalized parameters. Specific to the current 2D axisymmetric simulation, acoustic spectral and POD methodologies are used to investigate the unsteady behavior of the complex flow. Results have shown that oscillations of the stand-off shock may be one of the triggers for the acoustic generation, which agrees with Henderson and Powell's hypothesis [4].

Acknowledgement

The authors gratefully thank the financial support of the Australian Research Council (ARC).

References

[1] Chan, L., Chin, C., Soria, J. and Ooi, A., Large eddy simulation and reynolds-averaged navier-stokes calculations of supersonic impinging jets at varying nozzle-to-wall distances and impinging angles, *Int. J. Heat Fluid Flow.*, **47**, 2014, 31–41.

[2] Dauptain, A., M. Gicquel, L. and Moreau, S., Large eddy simulation of supersonic impinging jets, *AIAA J.*, **50**, 2012, 1560–1574.

[3] Henderson, B., The connection between sound production and jet structure of the supersonic impinging jet, *J. Acoust.*

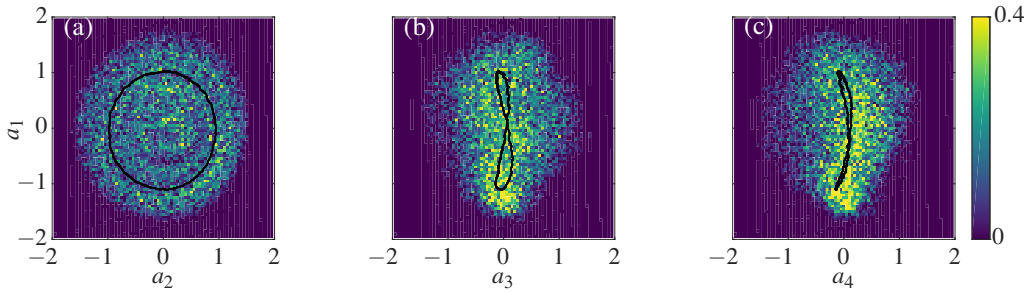

Figure 6: Joint PDFs of normalized POD coefficient pairs with overlaid Lissajous lines ranging from 0 to 0.4. (a) is the phase portrait of coefficients a_1 and a_2, followed by that of coefficients a_1 and a_3 in (b) and coefficients a_1 and a_4 in (c). A solid black line in each graph is indicative of the Lissajous line.

Soc. Am., **111**, 2002, 735–747.

[4] Henderson, B. and Powell, A., Experiments concerning tones produced by an axisymmetric choked jet impinging on flat plates, *J. SOUND VIB.*, **168**, 1993, 307–326.

[5] Ho, C.-M. and Nosseir, N. S., Dynamics of an impinging jet. part 1. the feedback phenomenon, *J. Fluid Mech.*, **105**, 1981, 119–142.

[6] Kim, S. I. and Park, S. O., Oscillatory behavior of supersonic impinging jet flows, *Shock Waves.*, **14**, 2005, 259–272.

[7] Marsh, A. H., Noise measurements around a subsonic air jet impinging on a plane, rigid surface, *J. Acoust. Soc. Am.*, **33**, 1961, 1065–1066.

[8] Oberleithner, K., Sieber, M., Nayeri, C., Paschereit, C., Petz, C., Hege, H.-C., Noack, B. and Wygnanski, I., Three-dimensional coherent structures in a swirling jet undergoing vortex breakdown: stability analysis and empirical mode construction, *J. Fluid Mech.*, **679**, 2011, 383–414.

[9] Powell, A., The sound-producing oscillations of round underexpanded jets impinging on normal plates, *J. Acoust. Soc. Am.*, **83**, 1988, 515–533.

[10] Risborg, A., High speed optical investigation of shock-wave instabilities in an underexpanded impinging jet, *Honours Thesis.*.

[11] Schmid, P. J., Dynamic mode decomposition of numerical and experimental data, *J. Fluid Mech.*, **656**, 2010, 5–28.

[12] Sirovich, L., Turbulence and the dynamics of coherent structures. i. coherent structures, *Quart. Appl. Math.*, **45**, 1987, 561–571.

[13] Weightman, J. L., Amili, O., Honnery, D., Soria, J. and Edgington-Mitchell, D., An explanation for the phase lag in supersonic jet impingement, *J. Fluid Mech.*, **815**.

[14] Wilke, R. and Sesterhenn, J., On the origin of impinging tones at low supersonic flow, *arXiv preprint arXiv:1604.05624*.

[15] Zang, B., US, V. and New, T. H. D., Openfoam based numerical simulation study of an underexpanded supersonic jet, in *55th AIAA Aerospace Sciences Meeting.*, 2017, 0747, 0747.

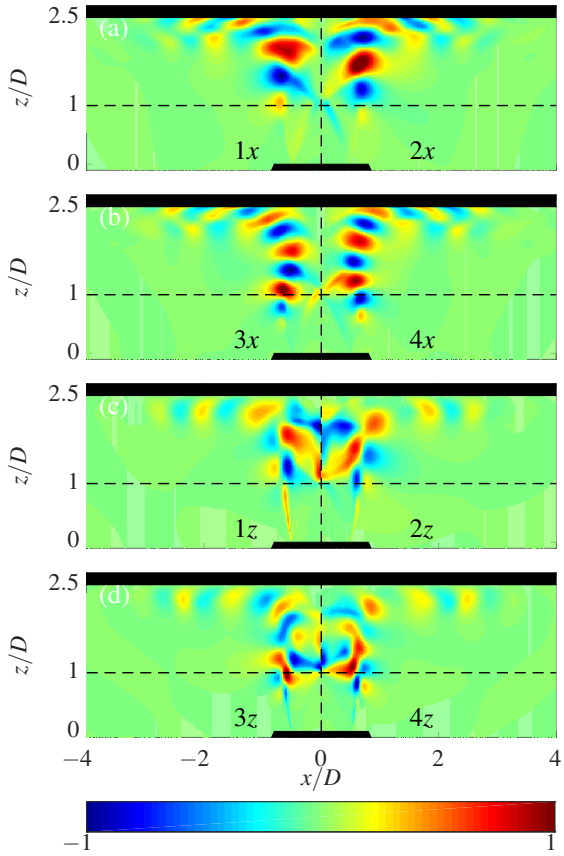

Figure 7: The first four POD modes based on the radial (x) velocity field in (a) and (b), and stream-wise (z) velocity field in (c) and (d). (a) and (c) represent the first two POD modes, whilst (b) and (d) do the last two POD modes.

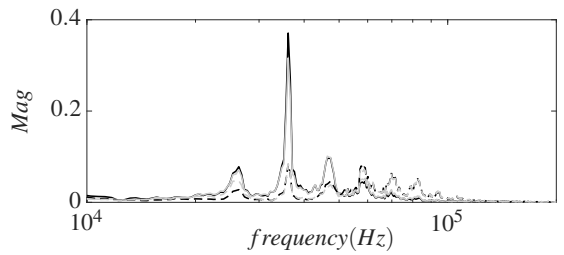

Figure 8: Magnitudes of normalized POD coefficients as a function of frequency, in which ——: a_1, ——: a_2, - - -: a_3, - - -: a_4.